2022-01-30

Godunov-type large time step scheme for shallow water equations with bed-slope source term

Xu, R

10.1016/j.compfluid.2021.105222
Computers and Fluids
Elsevier

Godunov-type Large Time Step scheme for Shallow Water Equations with Bed-Slope Source Term

Renyi Xu[1*], Alistair G. L. Borthwick[2,3], Hongbo Ma[4*], Bo Xu[1]

1 College of Hydraulic Science and Engineering, Yangzhou University, China

2 School of Engineering, The University of Edinburgh, Edinburgh, UK

3 School of Engineering, Computing and Mathematics, University of Plymouth, Plymouth, UK

4 Department of Environmental Sciences, University of Virginia, USA

*Corresponding authors: xury@yzu.edu.cn (R. Xu) and bigmatton@gmail.com (H. Ma)

Abstract: This paper presents a Godunov-type large time step (LTS) solver of the non-homogeneous shallow water equations (SWEs). Source terms are decomposed into simple characteristic waves in approximate Riemann solvers (ARS) and exact Riemann solvers (ERS), and information is transferred over multiple cells per time step using the LTS method. Benchmark simulations are presented using different solution algorithms (ARS and ERS with and without entropy fixes) for two rarefactions driven by divergent flow, a pair of bores driven by opposing flows, and a dam break over a shelf-like step. In these cases, spurious flow discontinuities and oscillations can occur for Courant–Friedrichs–Lewy number (CFL) > 1 in the absence of an entropy fix. Implementation of a weak-solution LTS entropy fix improves the results, but shock shifting nevertheless occurs in certain cases. The paper also considers steady, frictionless, transcritical flow over a bed hump. In this final case, the model is run for integer CFL ranging from 1 to 10. For CFL ≤ 3, satisfactory results are obtained (without divergence and oscillation) using ARS without an entropy fix. For larger CFL, the results either diverge or exhibit convergent oscillations downstream of the hydraulic jump. Use of an entropy fix designed for implementation in an LTS scheme improves the results for CFL ≤ 5.

Keywords: Large Time Step scheme, Shallow Water Equations, Step Riemann Solver, oscillation suppression

1. Introduction

Advection-dominated shallow environmental flows may exhibit high, even discontinuous, gradients in free surface elevation, flow velocity, and material transport fluxes. Particular examples include the hydraulic jump in an open channel that occurs as the flow transitions from supercritical to subcritical conditions, the hydraulic bore caused by a dam break or tidal incursion into a river, and steep-fronted flows that characterize urban flood inundation. Theoretical analysis of such flows requires solving conservation laws for mass and momentum expressed as hyperbolic systems with source and sink terms representing bed gradient, frictional, and other effects (see e.g. Abbott and Minns [1] and Cunge et al. [2]). Since the 1980s, many approximate Riemann solvers (ARS) have been proposed for such hyperbolic systems following the pioneering work of Roe [3], including schemes by Osher and Solomon [4], Harten et al. [5], and Liou and Christopher [6], and summarized

in books by Toro [7, 8], LeVeque [9] and Guinot [10], and reviews by Toro and García-Navarro [11], etc. The majority of these schemes are restricted by the Courant–Friedrichs–Lewy (CFL) condition (CFL = $c\Delta t/\Delta x < 1$ where c is the wave celerity, Δt is the time step and Δx is the spatial step), which requires a very small time step that reduces computational efficiency.

In 1982, LeVeque [12] devised a Godunov-type (LTS) scheme that overcame the CFL constraint in a first-order upwind difference solver used to simulate one-dimensional shock wave propagation. The essence of this work (thus LTS) was to track the influence of a single computational interface through multiple adjacent cells, while the conventional method forbids the interface to pass through even one cell, i.e. CFL < 1. The more cells the solver can track through, the more relaxed the CFL condition could be. Soon afterwards, Harten [13] applied the LTS scheme within a total-variation diminishing (TVD) solver of the Euler equations, and demonstrated its applicability to a shock wave in gas dynamics. In 1988, LeVeque [14] extended his original scheme to two-dimensions and second order accuracy, and presented results for obliquely propagating shock waves. Even though the scheme is highly efficient computationally, it has not been as widely implemented as classical schemes. In 2006, Murillo et al. [15] applied the LTS scheme to solving the shallow water equations and demonstrated its effectiveness in simulating various benchmark cases of steady and transient flows including dam breaks and a hydraulic jump. Meanwhile, Qian and Lee used LTS to solve the Euler equations in aerodynamics for inviscid flow past airfoils [16] and later extended the method to TVD schemes [17]. Recently, Xu et al. [18] devised a method to suppress spurious oscillations in a LTS scheme for an ERS of the shallow water equations (SWEs), and accurately reproduced dam break flows for CFL up to 25. Morales-Hernández et al. [19] developed a two-dimensional LTS scheme for the SWEs that handled wetting and drying, which they applied to a circular dam break, a dam break over an adverse slope, a tsunami interacting with a beach, and a flood event induced by dam failure in the Ebro River. Lindqvist et al. [20] compared the performance of several LTS-TVD schemes and examined numerical entropy fixes for application to generalized transonic rarefactions in nonlinear systems. The foregoing discussion relates solely to the use of LTS in Godunov-type solvers of homogenous hyperbolic partial equations.

In practice, there are many cases involving additional source terms, such as ones related to wind and bed friction stresses, Coriolis acceleration from the rotation of the Earth, bed porosity as a momentum source term, etc. It is well established that variable depth as a source term has implications for the correct balancing of the scheme, such as the dam break over a bed hump considered by LeVeque [21]. In general, the conservation properties of a Godunov-type shallow flow solver can be jeopardized by incorrect treatment of source terms in the shallow water equations related to flow geometry. According to Garcia-Navarro and Vazquez-Cendon [22] damage can be caused to the conservation properties of the scheme through careless treatment of source terms related to the flow geometry. Bed and wind friction stresses are commonly introduced as source terms in the shallow water equations. In such cases, the equations can become computationally stiff, and are handled using implicit schemes [23], and fractional step and f-wave methods [24].

Herein, we extend the principle of LTS to SWEs with the bed-slope source term. Recalling the principle of LTS, we focus on incorporating source terms into a Riemann solver such that the Riemann solver can accurately track the influence of the source term (together with interfacial waves) from one interface through multiple adjacent cells. The major challenge consists of two problems. The first problem is to find or develop a proper Riemann solver for SWEs with source terms and the second is to examine whether such a Riemann solver can incorporate the LTS method. In general,

Godunov-type schemes for shallow water equations with the bed-slope source term can be discretized into a series of local step Riemann problems (SRPs). Each SRP is solved using either an ARS or ERS. Murillo and García-Navarro [25] used an augmented Riemann solver to solve the SRPs as multiple states for the shallow water equations with source terms. Based on different conservation principles (mass or momentum), multiple ERSs for local SRPs were proposed for shallow flow over a non-uniform bed [26, 27]. Bernetti et al. [28] treated the channel bed as an additional equation, and the enlarged hyperbolic system thus enabled both mass and momentum conservations to be considered at the same time. Based on the enlarged equation set, Bernetti et al. derived a new ERS. However, this ERS assumes some prior knowledge of the wave structure, and so its generalization is challenging. Rosatti et al. [29] further showed that the wave generated at the bed discontinuity is in fact a contact wave, across which Riemann invariants do not hold, rendering the foregoing ERSs questionable, especially under the condition of a negative step bed. To date, previous studies have not provided a satisfactory ERS for shallow flow on the non-uniform bed. With the aim to enable LTS for SWEs with bed-slope source term, we firstly develop a new ERS, based on the governing equation set derived by Rosatti et al.[29], but not requiring prior knowledge of wave structures, and then we derive LTS algorithms from the new ERS and an existing ARS for SWEs with the bed-slope source term so that we can evaluate their performance under multiple benchmark scenarios.

The paper is structured as follows. Section 2 presents the governing shallow water equations with a bed-slope source term in hyperbolic matrix-vector form. Section 3 describes the ARS and ERS used to evaluate the local step Riemann problems, and gives details of the LTS scheme employed to accelerate the solver, and entropy fixes used to minimize spurious oscillations and discontinuities in the solutions. Section 4 presents results obtained for several unsteady, transcritical flows over a step, and steady, transcritical flow over a bed hump. Section 5 lists the main findings.

2. Governing Equations

Consider shallow flow in one spatial dimension. Assuming the pressure is hydrostatic, the inviscid shallow water equations with a bed-slope source term obtained from mass and momentum conservation laws (see e.g. [8]) may be written in matrix-vector form as follows:

$$\frac{\partial \boldsymbol{U}}{\partial t}+\frac{\partial \boldsymbol{F}(\boldsymbol{U})}{\partial x}=\boldsymbol{S}_f \tag{1}$$

$$\boldsymbol{U}=\begin{bmatrix} h \\ hu \end{bmatrix}, \boldsymbol{F}(\boldsymbol{U})=\begin{bmatrix} hu \\ hu^2+\frac{1}{2}gh^2 \end{bmatrix}, \boldsymbol{S}_f=\begin{bmatrix} 0 \\ gh\frac{\partial z}{\partial x} \end{bmatrix}$$

where $\boldsymbol{U}$ is the vector of dependent variables, $\boldsymbol{F}(\boldsymbol{U})$ is the horizontal flux vector, $\boldsymbol{S_f}$ is the vector of source terms, t is time, x is downstream distance along the channel, h is the local water depth measured vertically from the bed to the free surface, u is the local bulk flow velocity, g is gravitational acceleration, and z is the bed elevation above a fixed horizontal datum.

3. Numerical Model

3.1 Step Riemann Problem

Fig. 1 depicts the varying water level and bed profile along a one-dimensional open channel of constant, unit width with frictionless lateral walls. The flow domain is discretized using finite volumes, as shown in Fig. 2, such that the grid is regular, and distance $x = i\Delta x$ where Δx is the spatial grid increment. During the numerical solution process, each interface between neighboring cells comprises a local step Riemann problem (SRP), as exemplified by the interface (indicated by an arrow) between the ith and i+1th cell.

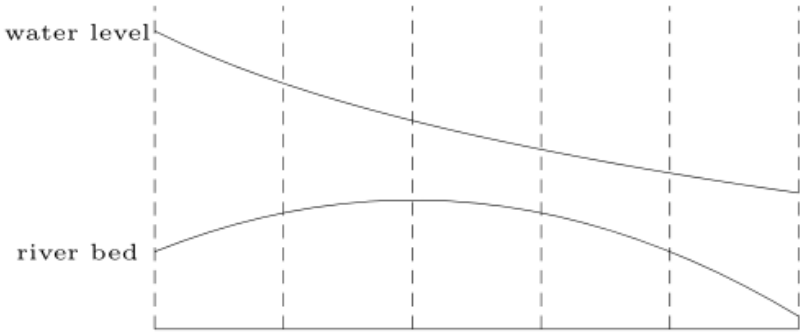

Fig. 1 Schematic of bed and free surface elevation profiles along a one-dimensional channel

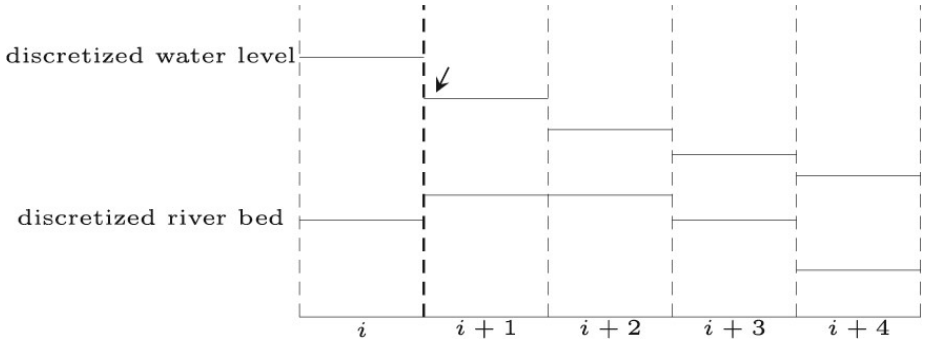

Fig. 2 Finite volume discretization in the vicinity of the ith computational cell

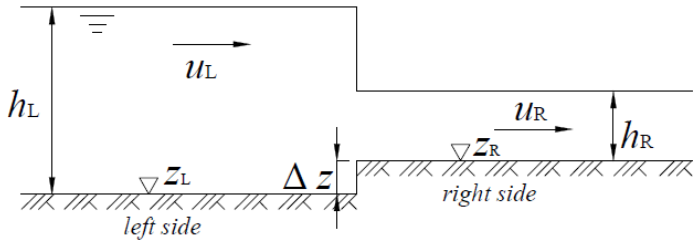

Fig. 3 Close-up view of the step Riemann problem at a cell interface

3.1.1 Approximate Riemann Solver

Fig. 3 provides a close-up view of the SRP, and shows a step in the bed of height Δz, where the depth, velocity, and bed elevation are given by (h_L , U_L, z_L) to the left of the step (upsteam) and (h_R , U_R, z_R) to the right of the step (downstream). The cell interface occurs at the bed gradient discontinuity (i.e. the step itself). To solve this problem, equation (1) is converted into quasi-linear form following Rosatti and Begnudelli [29], giving:

$$\frac{\partial \boldsymbol{U}'}{\partial t} + \boldsymbol{A}\frac{\partial \boldsymbol{U}'}{\partial x} = 0 \tag{2}$$

where the modified vector of dependent variables is

$$\boldsymbol{U}' = \begin{bmatrix} h \\ hu \\ z \end{bmatrix}$$

and the flux Jacobian matrix $\boldsymbol{A}$ is characterized by

$$\det\left|\boldsymbol{A} - \lambda_i \boldsymbol{I}\right| = 0; \quad \boldsymbol{AR} = \lambda_i \boldsymbol{R} \tag{3}$$

with eigenvalues

$$\lambda_1 = u - c; \quad \lambda_2 = 0; \quad \lambda_3 = u + c \tag{4}$$

and the right-hand eigenvector matrix

$$\boldsymbol{R} = \begin{bmatrix} 1 & a & 1 \\ u - c & 0 & u + c \\ 0 & u^2 - c^2 & 0 \end{bmatrix} \tag{5}$$

Here, u and c are Roe averages of connected cells either side of the stepped interface (Fig. 3). Letting i represent the left cell and i+1 the right cell, then the Roe-averaged depth and wave celerity, u and c, are given as:

$$u = \frac{u_L\sqrt{h_L} + u_R\sqrt{h_R}}{\sqrt{h_L} + \sqrt{h_R}} \tag{6}$$

and

$$c = \sqrt{\frac{g\left(h_L + h_R\right)}{2}} \tag{7}$$

In Eq(5), a is defined:

$$a = g\left(h_k - \frac{\left|z_R - z_L\right|}{2}\right) \text{ where } h_k = \begin{cases} h_L, z_L \le z_R \\ h_R, z_L > z_R \end{cases} \tag{8}$$

The LTS scheme requires information on the wave strength, defined as the difference in the

modified vector of dependent variables between adjacent cells, as follows:

$$\Delta \boldsymbol{U}'=\begin{cases}\Delta h = h_R - h_L \\ \Delta(hu) = h_R u_R - h_L u_L \\ \Delta z = z_R - z_L\end{cases} \tag{9}$$

The wave strength is also related to the eigenspace, such that:

$$\Delta \boldsymbol{U}'=\begin{bmatrix}\alpha_1 & \alpha_2 & \alpha_3\end{bmatrix}\boldsymbol{R} \tag{10}$$

where the coefficients in the row vector are given by:

$$\begin{cases}\alpha_1 = \dfrac{\lambda_3 \Delta h - \Delta(hu)}{2\%} - \dfrac{a\Delta z}{2\%\lambda_1} \\ \alpha_2 = \dfrac{\Delta z}{\lambda_1 \lambda_3} \\ \alpha_3 = -\dfrac{\lambda_1 \Delta h - \Delta(hu)}{2\%} - \dfrac{a\Delta z}{2\%\lambda_3}\end{cases} \tag{11}$$

3.1.2 Exact Riemann Solver

Fig. 4 illustrates one of four possible Riemann solutions for the SRP. At the step, a static shock occurs with zero celerity. Either side of the static shock, the variables u_{SL}, h_{SL}, u_{SR} and h_{SR} are unknown and can be determined from relations with known variables u_L, h_L, z_L, u_R, h_R.

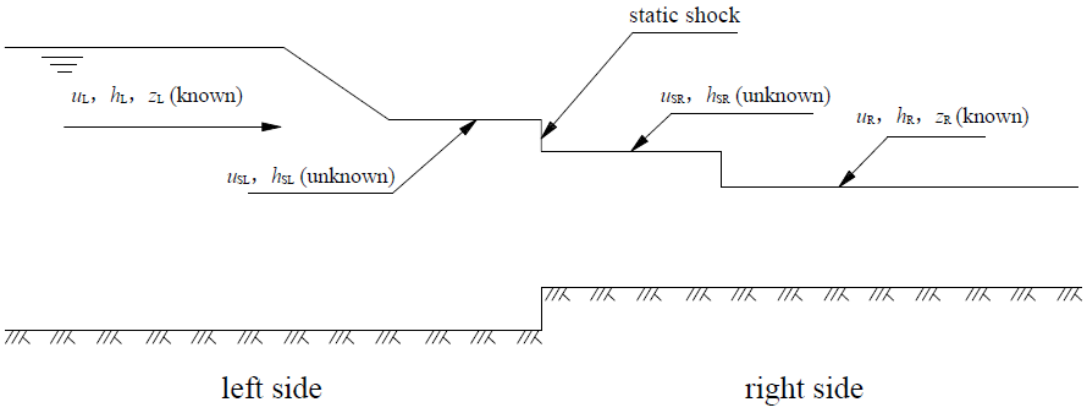

Fig. 4 Riemann solution for shallow flow over a step

If the left side is a rarefaction wave, then the Riemann invariants are:

$$u_L + 2\sqrt{gh_L} = u_S + 2\sqrt{gh_S} \tag{12}$$

If the left side is a shock, the Riemann invariants are:

$$\begin{cases} h_L u_L - h_{SL} u_{SL} = s\left(h_L - h_{SL}\right) \\ \left(h_L u_L^2 + \frac{1}{2} g h_L^2\right) - \left(h_{SL} u_{SL}^2 + \frac{1}{2} g h_{SL}^2\right) = s\left(h_L u_L - h_{SL} u_{SL}\right) \end{cases} \tag{13}$$

in which s is the speed of the shock.

If the right side is a rarefaction wave, then:

$$u_R - 2\sqrt{gh_R} = u_S - 2\sqrt{gh_S} \tag{14}$$

If the right side is a shock, then:

$$\begin{cases} h_R u_R - h_{SR} u_{SR} = s\left(h_R - h_{SR}\right) \\ \left(h_R u_R^2 + \frac{1}{2} g h_R^2\right) - \left(h_{SR} u_{SR}^2 + \frac{1}{2} g h_{SR}^2\right) = s\left(h_R u_R - h_{SR} u_{SR}\right) \end{cases} \tag{15}$$

The static shock satisfies the relationships:

$$h_{SL} u_{SL} = h_{SR} u_{SR} \tag{16}$$

$$h_{SL} u_{SL}^2 + \frac{1}{2} g h_{SL}^2 = h_{SR} u_{SR}^2 + \frac{1}{2} g h_{SR}^2 + D \tag{17}$$

in which

$$D = g\left(h_k - \frac{\left|Z_R - Z_L\right|}{2}\right)\left(Z_R - Z_L\right), k = \begin{cases} L & Z_L \le Z_R \\ R & Z_L \ge Z_R \end{cases} \tag{18}$$

Table 1 summarizes the Riemann states for the SRP [29]:

	Right-middle-left	Abbr.	equations
1	Rarefaction-static shock-shock	RBS	(12)(16)(17)(15)
2	Shock-static shock-shock	SBS	(13)(16) (17)(15)
3	Rarefaction-static shock-Rarefaction	RBR	(12)(16) (17)(14)
4	Shock-static shock-Rarefaction	SBR	(13) (16) (17)(14)

Table 1 Equations of Riemann solver

The resulting 4-6 nonlinear equations are solved numerically using the Levenberg-Marquardt method (code available from https://www.math.utah.edu/software/minpack.html). To determine the Jacobi matrix, the equations are simplified to a pair of right hand conditions, each of which is divided into two sub-conditions (comprising four Riemann invariants). First, we define the following variables:

$$\begin{cases} D_1=u_L+2\sqrt{gh_L} \\ D_2=u_L-2\sqrt{gh_L} \\ D_3=\sqrt{\frac{1}{2}\frac{h_{LS}+h_L}{gh_{LS}h_L}} \\ D_4=\left(h_R u_R^2+\frac{1}{2}gh_R^2\right) \\ D_5=h_R u_R \\ D_7=u_R-2\sqrt{gh_R} \end{cases} \tag{19}$$

If the left side is a rarefaction, the variables are calculated from Eq (12) as.

$$\begin{cases} u_{LS}=D_1-2\sqrt{gh_{LS}} \\ \frac{\partial u_{LS}}{\partial h_{LS}}=-\sqrt{\frac{g}{h_{LS}}} \end{cases} \tag{20}$$

If left side is a shock, the variables are calculated from Eq (13) as

$$\begin{cases} u_{LS}=u_L-\left(h_{LS}-h_L\right)D_3 \\ \frac{\partial u_{LS}}{\partial h_{LS}}=-D_3+\frac{\left(h_{LS}-h_L\right)}{4D_3h_{LS}^2} \end{cases} \tag{21}$$

When the right side is a rarefaction, then, according to Eq(14):

$$\begin{cases} u_{RS}=D_7+2\sqrt{gh_{RS}} \\ \frac{\partial u_{RS}}{\partial h_{RS}}=\sqrt{\frac{g}{h_{RS}}} \end{cases} \tag{22}$$

And according to Eqs (16) and (17),

$$\begin{cases} f_1=h_{LS}u_{LS}-h_{RS}u_{RS} \\ f_2=h_{LS}u_{LS}^2+\frac{1}{2}gh_{LS}^2-h_{RS}u_{RS}^2-\frac{1}{2}gh_{RS}^2-D \end{cases} \tag{23}$$

When the left side is a rarefaction, the Levenberg-Marquardt method is configured as follows:

$$\begin{cases} f_1\left(h_{LS},h_{RS}\right)=0 \\ f_2\left(h_{LS},h_{RS}\right)=0 \\ \dfrac{\partial f_1}{\partial h_{LS}}=u_{LS}+h_{LS}\dfrac{\partial u_{LS}}{\partial h_{LS}} \\ \dfrac{\partial f_1}{\partial h_{RS}}=\text{-}u_{RS}-h_{RS}\dfrac{\partial u_{RS}}{h_{RS}} \\ \dfrac{\partial f_2}{\partial h_{LS}}=u_{LS}^2+2h_{LS}u_{LS}\dfrac{\partial u_{LS}}{\partial h_{LS}}+gh_{LS}-g\Delta z \\ \dfrac{\partial f_2}{\partial h_{RS}}=-u_{RS}^2-2h_{RS}u_{RS}\dfrac{\partial u_{RS}}{\partial h_{RS}}-gh_{RS} \end{cases} \tag{24}$$

When the right side is a shock, according to Eq (16):

$$\begin{cases} u_{RS}=\dfrac{h_{LS}u_{LS}}{h_{RS}} \\ \dfrac{\partial u_{RS}}{\partial h_{LS}}=\dfrac{u_{LS}+h_{LS}\dfrac{\partial u_{LS}}{\partial h_{LS}}}{h_{RS}} \\ \dfrac{\partial u_{RS}}{\partial h_{RS}}=-\dfrac{h_{LS}u_{LS}}{h_{RS}^2} \end{cases} \tag{25}$$

And from Eq (15):

$$f_3=\left[D_5-h_{LS}u_{LS}\right]^2-\left(h_R-h_{RS}\right)\left[D_4-\left(h_{RS}u_{RS}^2+\frac{1}{2}gh_{RS}^2\right)\right] \tag{26}$$

When the left side is a shock, the Levenberg-Marquardt method is configured as follows:

$$\begin{cases} f_3\left(h_{LS},h_{RS}\right)=0 \\ f_2\left(h_{LS},h_{RS}\right)=0 \\ \dfrac{\partial f_3}{\partial h_{LS}}=-2\left[D_5-h_{LS}u_{LS}\right]\left(h_{LS}\dfrac{\partial u_{LS}}{\partial h_{LS}}+u_{LS}\right)+2\left(h_R-h_{RS}\right)h_{RS}u_{RS}\dfrac{\partial u_{RS}}{\partial h_{LS}} \\ \dfrac{\partial f_3}{\partial h_{RS}}=\left[D_4-\left(h_{RS}u_{RS}^2+\dfrac{1}{2}gh_{RS}^2\right)\right]+\left(h_R-h_{RS}\right)\left(u_{RS}^2+2h_{RS}u_{RS}\dfrac{\partial u_{RS}}{\partial h_{RS}}+gh_{RS}\right) \\ \dfrac{\partial f_2}{\partial h_{LS}}=u_{LS}^2+2h_{LS}u_{LS}\dfrac{\partial u_{LS}}{\partial h_{LS}}+gh_{LS}-2h_{RS}u_{RS}\dfrac{\partial u_{RS}}{\partial h_{LS}}-g\Delta z \\ \dfrac{\partial f_2}{\partial h_{RS}}=-u_{RS}^2-2h_{RS}u_{RS}\dfrac{\partial u_{RS}}{\partial h_{RS}}-gh_{RS} \end{cases} \tag{27}$$

The ARS described in Section 0 is used to decide whether the state either side of the step relates to a shock or rarefaction before using the Levenberg-Marquardt method. The eigenvalues are

$$\lambda_L=u_L-\sqrt{gh_L} \tag{28}$$

$$\lambda_R = u_R - \sqrt{gh_R} \tag{29}$$

For $|\lambda_1| < |\lambda_L|$, the left side is

condition	result	condition	result
$\lvert\lambda_1\rvert < \lvert\lambda_L\rvert$	Left rarefaction	$\lvert\lambda_3\rvert < \lvert\lambda_R\rvert$	Right rarefaction
$\lvert\lambda_1\rvert > \lvert\lambda_L\rvert$	Left shock	$\lvert\lambda_3\rvert > \lvert\lambda_R\rvert$	Right shock

Table 2 Method of judging wave type

In Table 2, λ_1, λ_3 are determined from Eq (4). The procedure for solving the SRP follows:

$$\text{judge kind of wave by Table2} \rightarrow \begin{cases} \text{right shock,} & \text{Eq}(27) \\ \text{right rarefaction,} & \text{Eq}(24) \end{cases} \rightarrow \begin{cases} \text{left shock,} & \text{Eq}(21) \\ \text{left rarefaction,} & \text{Eq}(20) \end{cases}$$

Table 3 indicates the revised version of Table 1 that results,

	Right-middle-left	Abbr.	equations
1	Rarefaction-static shock-shock	RBS	(24) (20)
2	Shock-static shock-shock	SBS	(24) (21)
3	Rarefaction-static shock-Rarefaction	RBR	(27) (20)
4	Shock-static shock-Rarefaction	SBR	(27) (21)

Table 3 Equations used by Riemann solver for Step Riemann Problem

The Minpack of the Levenberg-Marquardt method is then configured.

3.2 Large Time Step Scheme

The version of SWEs considered herein forms a nonlinear hyperbolic system. To explain the updating method at the heart of the LTS scheme for nonlinear hyperbolic systems, we first consider the linear hyperbolic partial differential equation for pure advection,

$$\frac{\partial u}{\partial t} + \lambda \frac{\partial u}{\partial x} = 0 . \tag{30}$$

where u is a scalar dependent variable and λ is the advection wave speed. After discretization with the upwind method, equation (12) becomes

$$u_i^{n+1} = u_i^n - \frac{\lambda_i^n \Delta t}{\Delta x}\left(u_i^n - u_{i-1}^n\right) \tag{31}$$

where Δx is the space step, Δt is the time step, and λ_i^n is the wave advection speed at interface $x_{i-1/2}$ at time $t^n = n\Delta t$ (with $n = 0, 1, \ldots n_{\max}$). Over the time interval Δt, a simple wave advecting u from $x_{i-1/2}$ reaches the point ε at time t^{n+1} (see Fig. 5) and the wave travels a distance s given by:

$$s = \lambda \Delta t \,. \tag{32}$$

Traditional update methods require that Δt should not be so large that the simple wave exits the other cell interface at $x_{i+1/2}$, which means $s < \Delta x$. The LTS scheme overcomes this constraint, permitting the time step to be sufficiently large for the simple wave to enter a cell beyond the i+1/2 interface, as indicated in Fig. 6.

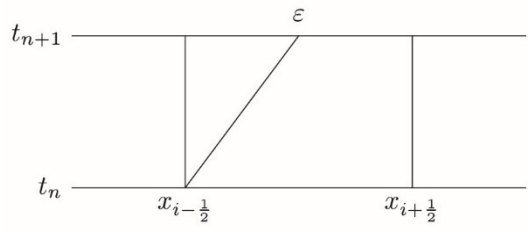

Fig. 5 *x-t* plot showing wave propagation in space and time for a conventional CFL limited scheme

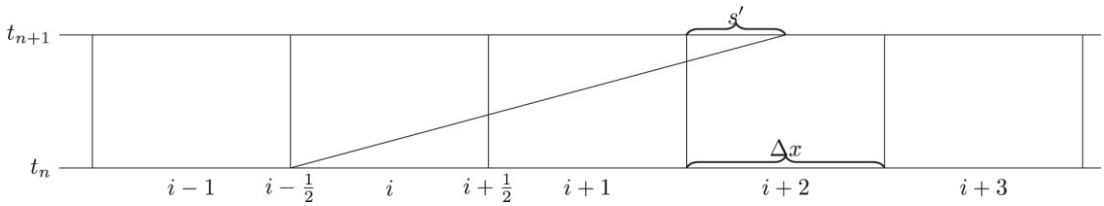

Fig. 6 *x-t* plot showing wave propagation in space and time for an LTS scheme

In practice, advection in space and time across the grid can be divided into two types:

Type a. The wave travels across the whole i th cell, in which case the wave propagates exactly the length of the cell, such that:

$$s_i = \Delta x_i \tag{33}$$

Type b. The wave travels part of the cell, such as in the i+2 th cell shown in Fig. 6, where the distance s' is obtained as:

$$s' = \lambda \Delta t - \left[\lambda \Delta t \right] \tag{34}$$

and the square brackets mean taking the integer part of the value of the variable within the brackets (for example, [6.5] is 6 and [-6.5] is -6.

To simplify the LTS update method, a further variable, ζ, is introduced as:

$$\zeta = \frac{s'}{\Delta x} \tag{35}$$

and the wave strength is defined as:

$$\Delta u = u_i - u_{i-1} \tag{36}$$

Hence, Eq. (18) becomes:

$$u_i^{n+1}=u_i^n-\zeta_i\Delta u_i \tag{37}$$

In short, Δu_i, ζ_i, and s are defined by equations (36), (35), (33) and (34), respectively. In LTS, the value of ζ_i is determined from:

$$\zeta=\begin{cases}1, & \text{simple wave travel through the whole cell}\\ \dfrac{s'}{\Delta x}, & \text{simple wave travel through part of the cell}\end{cases} \tag{38}$$

where s' is the travel instance in a given cell, as indicated in Fig. 6.

When the linear hyperbolic equation (Eq (30)) is expanded to the hyperbolic nonlinear system given by Eqs (1) or (2), multiple simple waves are generated at the interface between each pair of adjacent cells. The update method of LTS remains the same as Eq (37), except that the scalar dependent variable is replaced by the vector of dependent variables, and may be written,

$$\boldsymbol{U}^{n+1}=\boldsymbol{U}^n+\zeta\boldsymbol{\alpha} \tag{39}$$

where $\boldsymbol{U}$ is defined as in Eq (1) or Eq (2), and the vector $\boldsymbol{\alpha}$ is defined by Eq (11). The bed elevation, z, is a local constant in time and so is not updated. During implementation, only α_1 and α_3 are used to update h and hu. The variable ζ is defined by Eq (38). Then the celerity λ is evaluated from Eq (4) in order to determine which and how many cells contain information that requires updating as the wave passes through. Likewise, only λ_1 and λ_3 are used for updating h and hu.

3.3 Entropy fix

3.3.1 Exact solution of rarefaction

This method is to eliminate discontinuity in the rarefaction with ERS. The rarefaction fan comprises more than one wave. Fig. 7 shows a left rarefaction, demarked by leading and tail wave fronts [16, 18].

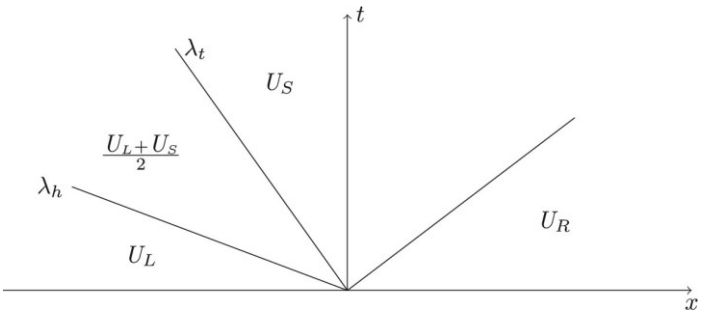

Fig. 7 *x-t* plot showing the splitting of the left rarefaction

The leading component of the rarefaction has speed,

$$\lambda_h=\lambda_L \tag{40}$$

in which λ_L is given by Eq (28). The rarefaction tail has speed,

$$\lambda_t = \lambda_1 \tag{41}$$

in which λ_1 is given by Eq(4). The Riemann state between the head and the tail is

$$\boldsymbol{U}_{t} = \frac{\boldsymbol{U}_L + \boldsymbol{U}_S}{2} \tag{42}$$

The strength of the rarefaction tail is

$$\Delta \boldsymbol{U}_t = \boldsymbol{U}_{t} - \boldsymbol{U}_S \tag{43}$$

The strength of the rarefaction head is

$$\Delta \boldsymbol{U}_h = \boldsymbol{U}_L - \boldsymbol{U}_{t} \tag{44}$$

Now, the left rarefaction may be expressed by two waves of speeds defined by Eq (40) and Eq (41), and strengths defined by Eq (43) and Eq (44). A similar approach is used for the right rarefaction.

3.3.2 Weak solution of approximate solver

This method is to eliminate discontinuity in the rarefaction with ARS. To do this, the shocks are split into two waves of speeds [25]:

$$\begin{cases} \lambda_a = \dfrac{\lambda_L + \lambda}{2} \\ \lambda_b = \dfrac{\lambda_R + \lambda}{2} \end{cases} \tag{45}$$

and wave strengths:

$$\begin{cases} \Delta \boldsymbol{U}_a = \dfrac{\lambda_b - \lambda}{\lambda_b - \lambda_a} \Delta \boldsymbol{U} \\ \Delta \boldsymbol{U}_b = \dfrac{\lambda - \lambda_a}{\lambda_b - \lambda_a} \Delta \boldsymbol{U} \end{cases} \tag{46}$$

3.3.3 LTS fix

An LTS fix is implemented to suppress spurious oscillation arising either with ERS or ARS. During the original LTS computations, $\dfrac{s'}{\Delta x}$ in Eq (38) is invariably less than unity. We therefore introduce the following modification:

$$\frac{s'}{\Delta x} = \begin{cases} 0, & \dfrac{s'}{\Delta x} < \delta \\ 1, & \text{else} \end{cases} \tag{47}$$

where δ is fixed to have a value between 0 and 1. In the cases considered herein, δ is set to 0.2.

3.4 Test algorithm

For verification purposes, we eventually need to determine which combination (and in what order) of the foregoing techniques achieves the best outcome. Table 4 summarize the resulting eight algorithms we consider. All 4 algorithms use the LTS method given by Eq. (37) to update values of the dependent variables at each cell in turn, where ζ is determined by Eq (38).

Algorithm.	Acronyms	Note
1	LTS-ERS	Godunov LTS algorithm based on exact Riemann solver
2	LTS-ARS	Godunov LTS algorithm based on approximate Riemann solver
3	LTS-ERS-EF	Godunov LTS algorithm based on exact Riemann solver with entropy fix(chapter 3.3)
4	LTS-ARS-EF	Godunov LTS algorithm based on approximate Riemann solver with entropy fix(chapter 3.3)

Table 4 Test Algorithms

4. Results and Discussion

4.1 Case 1: two rarefactions in a channel with a step

The first case examines diverging flow over a step in an otherwise horizontal channel of overall length 25 m. The step is 1 m high, and occupies the right hand side of the channel, such that $z = 0$ for $x < 12.5$ m and $z = 1$ m for $x \geq 12.5$ m. In the numerical model, the one-dimensional channel is divided into 250 regularly spaced cells of spatial increment $\Delta x = 0.1$ m. The time step is adaptively obtained from $\Delta t = Cr\, \Delta x / \lambda$ where Cr is a prescribed value of maximum CFL number, as part of the updating process. In this case, the initial time step is set to 0.01 s and alters with every succeeding time step. Table 5 lists the initial depth and flow conditions in the channel, which are discontinuous at the step. Immediately to the left of the step, there is an initial leftward flow of depth 8 m and speed 2 m/s. To the right, there is an initial rightward flow of depth 5 m and speed 7.1704 m/s.

	h(m)	q(m^2/s)	z(m)
Left ($0 \leq x < 12.5$ m)	8.0	-16.0	0
Right ($12.5 < x \leq 25$ m)	5.0	35.852	1

Table 5 Initial conditions for two rarefactions in a channel with a step

Fig. 8. shows the predicted free surface and discharge per unit width profiles obtained at time t =0.8 s using the four updating algorithms (see Table 4) and different CFL numbers. The predictions are superimposed on the exact solution [29]. The two upper-left panels of Fig. 8 show the free surface and discharge per unit width profiles obtained using Algorithm 1 for a maximum CFL value of 1. This is taken as the baseline case. The free surface profiles are in reasonable agreement with the analytical solution, and show the presence of a leftward travelling rarefaction head at $x = 4.0$ m and tail at $x = 9.4$ m, a stationary shock at the step, and rightward travelling rarefaction head at $x = 19.8$ m and tail at $x = 23.6$ m. Likewise, the predicted and exact mass flux profiles are in satisfactory agreement, except for slight over-prediction of the left rarefaction and a slight under-prediction of the right rarefaction. Increasing CFL to 4, leads to a discontinuity in both free surface elevation and

mass flux (evident in the two-upper right panels of Fig. 8). The second and the third rows of Fig. 8 present the corresponding results obtained using Algorithm 3, this time for CFL = 2, 4, 6 and 8. There is appreciably better agreement with the exact solution, confirming that the results are considerably enhanced when entropy fix is configured into the ERS. The fourth row of Fig. 8 displays profiles obtained using Algorithm 2 which demonstrate that ARS without an entropy fix leads to spurious discontinuities in rarefaction for CFL = 4. Again, implementation of the entropy fix cures the problem, as can be seen by the panels in the fifth and sixth rows of Fig. 8 for Algorithm 4 and CFL = 2, 4, 6 and 8 (but are not as accurate as for Algorithm 2).

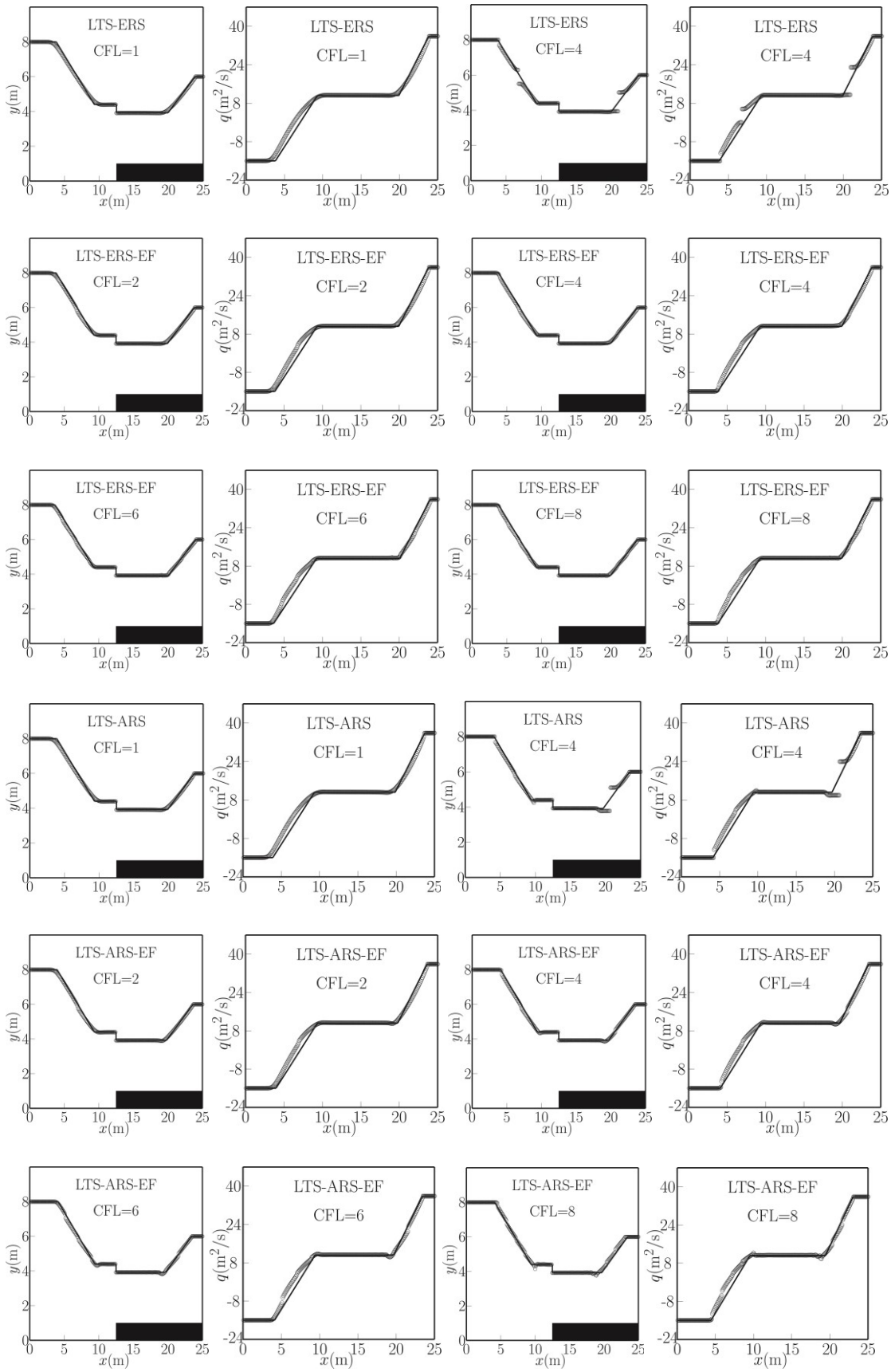

Fig. 8 Two rarefactions in a channel with a step. Exact solution (solid lines) and predicted (open circles) free surface and mass flux profiles at time t = 0.8 s. Bed shelf is the solid rectangle.

4.2 Case 2: two shock-like bores in a channel with a step

The second case corresponds to a tidal bore meeting a river flow. Again, the channel is 25 m long, and divided into 250 grid cells, each of spatial increment 0.1 m. The initial time step is 0.01 s, and altered thereafter according to the specified maximum CFL number. Table 6 lists the initial conditions, which comprise a rightward flow of depth 4 m and speed 4.75 m/s to the left of the step interface, and a leftward flow of depth 1.0838 m and speed 2.1854 m/s to the right of the step interface. We consider predictions obtained using algorithms outlines in Section 3.4.

	h(m)	q(m^2/s)	z(m)
Left ($0 \le x < 12.5$ m)	4.0	19	0
Right ($12.5 < x \le 25$ m)	1.0838	-2.3685	1

Table 6 Initial conditions for two shock-like bores in a channel with a step

Fig. 9 shows the free surface and mass flux profiles obtained at time 1.5 s using the four algorithms for different CFL numbers. Again, the predictions are superimposed on the exact solution [29]. The solution comprises a hydraulic drop at the step interface, a rightward propagating hydraulic bore at $x = 22.7$ m, and a leftward bore at $x = 8.2$ m. For Algorithm 1, the free surface and mass flux profiles are in reasonable agreement with the analytical solution when CFL = 1, the baseline case. Oscillations occur in both profiles in the right travelling bore when CFL = 4. For Algorithm 3, the oscillations are completely eliminated but the bore shifts from the correct position owing to numerical dispersion when CFL = 2 and 4. For CFL = 8, the dispersion problem is no longer evident, but both water surface and mass flux profiles contain spurious undulations. The dispersion problem and oscillation both occur when CFL = 6. For Algorithm 2, small oscillations occur in both profiles in the right travelling bore when CFL = 4. Use of the weak entropy fix in Algorithm 4, does not overcome this problem when CFL = 4 and worsens when CFL gets larger. Bore shifting does not occur when this algorithm is implemented, unlike Algorithm 3.

The numerical amplification factor is less than 1 (for more details see the Appendix, following [30, 31]), and so the LTS scheme is stable for linear hyperbolic equations. In the nonlinear system, wave celerities are not uniform at adjacent interfaces, and the wave strengths cannot be offset like Eq. (A1) (as mentioned for **Type a**., the coefficient is 1 if and only if the local celerity > 1). Then excessive information from boundary cells accumulates at inner cells inducing oscillation in the solution [32].

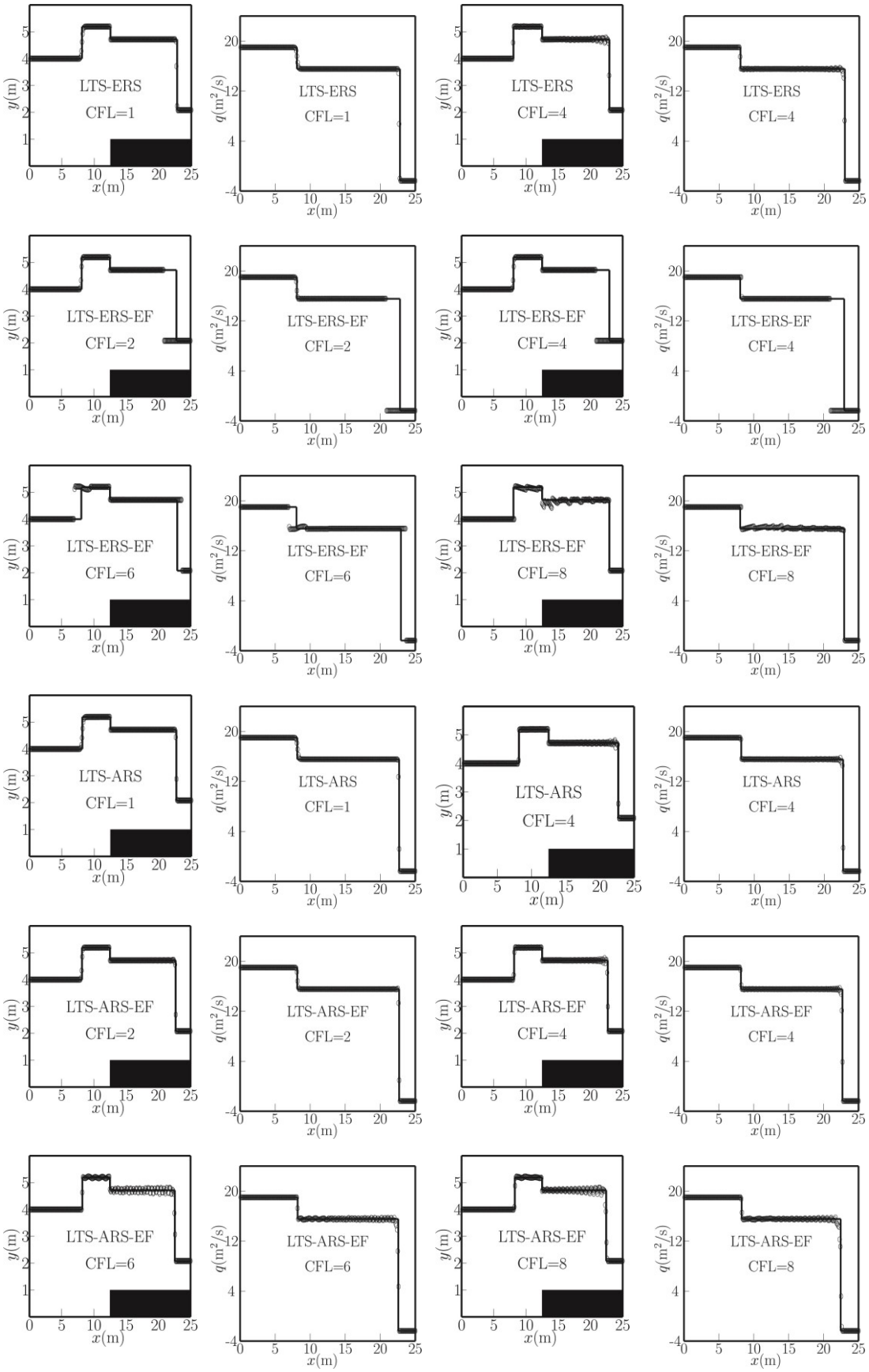

Fig. 9 Two shock-like bores in a channel with a step. Exact solution (solid lines) and predicted (open circles) free surface and mass flux profiles at time t = 1.5 s. Bed shelf is the solid rectangle.

4.3 Case 3: rarefaction and shock-like bore in a channel with a step

This case corresponds to a dam break over an otherwise quiescent wet bed. Again, the channel is 25 m long, and divided into 250 grid cells. Table 7 lists the initial flow conditions either side of the step interface. The initial time step is set to 0.01 s.

	h(m)	q(m^2/s)	z(m)
Left ($0 \leq x < 12.5$ m)	5.0	0	0
Right ($12.5 < x \leq 25$ m)	1.0	0	1

Table 7 Initial conditions for dam break in a channel with a step

Fig. 10 shows the water surface and mass flux profiles obtained at time t = 1.5 s, using the four algorithms (see Table 4) for different CFL numbers. Predictions are superimposed on the exact solution [29]. Here, the solution comprises a hydraulic drop at the step interface, a rightward propagating hydraulic bore at x = 21.47 m, and a leftward rarefaction head at x = 2.0 m and tail at x = 6.6 m. For Algorithm 1, the free surface and mass flux profiles are in reasonable agreement with the analytical solution when CFL = 1, the baseline case. It can be seen that the rarefaction becomes discontinuous when CFL value of 4. For Algorithm 3, the discontinuity of the rarefaction is cured because the configuration of entropy fix (Eqs (40)-(44)) and the oscillations are entirely eliminated with entropy fix (Eq. (47)) which can be seen in the second and third rows of Fig. 10 for CFL = 2, 4, 6 and 8. However, the bore shifts from the correct position as in Case 2 for Algorithm 3. The fourth row of Fig. 10 shows the profiles obtained using Algorithm 2. Again, the free surface and mass flux profiles are in reasonable agreement with the analytical solution when CFL = 1, the rarefaction is discontinuous, and oscillation appears for CFL = 4. The fifth and the sixth rows of Fig. 10 display profiles obtained using Algorithm 4, and it is evident that use of the weak solution entropy fix improves the predicted rarefaction but does not entirely eliminate the discontinuity.

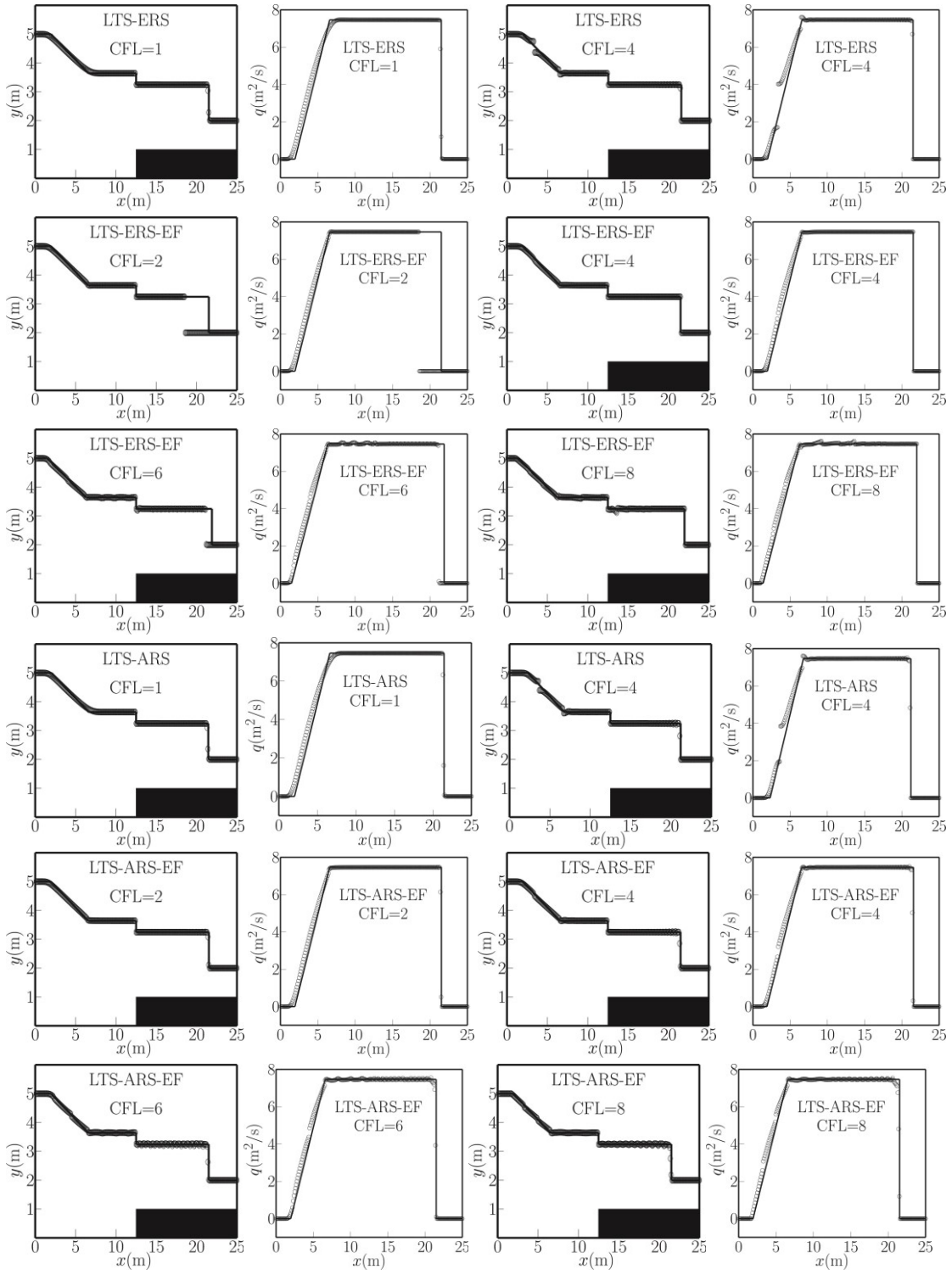

Fig. 10 Rarefaction and shock-like bore in a channel with a step. Exact solution (solid lines) and predictions (open circles) free surface and mass flux profiles at time t = 1.5 s. Bed shelf is the solid rectangle.

4.4 Transcritical flow over a fixed bed hump

The Godunov-type LTS solver is finally tested for the benchmark case of shallow, transcritical flow over a bed hump in a channel of overall length 25 m, originally proposed by Goutal and Maurel [33]. Fig. 11 shows the initial conditions, where the free surface elevation is set to a uniform value of 0.33 m above the $z = 0$ datum, and the bed level is specified such that:

$$\begin{cases} z = 0.2 - 0.05\left(x - 10\right)^2, & 8 < x \le 12 \\ z = 0, & \text{otherwise} \end{cases} \tag{48}$$

At the upstream open boundary, the discharge is 0.18 m^3/s, and at the downstream boundary, the water level is set to a constant value of 0.33 m above the $z = 0$ datum. Fig. 12 presents the analytical solution [33] for shallow flow over the hump, which accelerates from subcritical conditions to become supercritical on the downward slope of the hump before abruptly increasing in depth at a hydraulic jump, after which the flow is subcritical again. In this case, the ERS is unable to achieve a converged result because the relationship is unknown when the left bed is higher than the right bed elevation at a step [29]. Hence, the results presented here are obtained using an ARS using Algorithm 2 (see Section 3.4) and its version after the entropy fixes have been applied, Algorithm 4 (see Section 3.4).

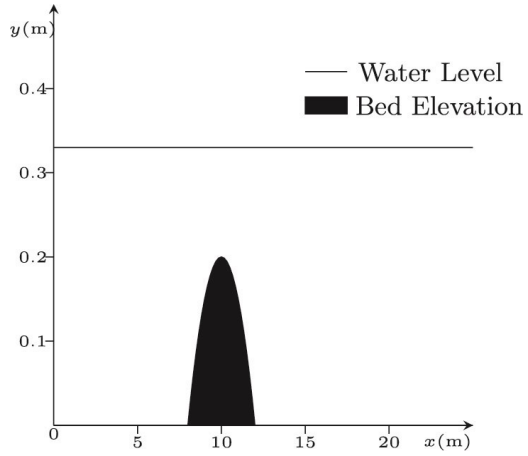

Fig. 11 Transcritical flow over a bed hump: initial free surface and bed elevation profiles

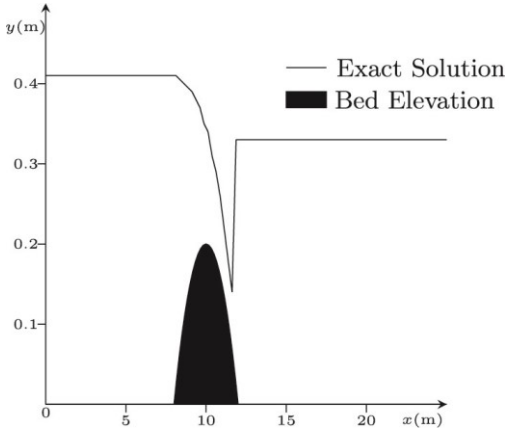

Fig. 12 Transcritical flow over a bed hump: analytical steady state free surface elevation profile[33]

In the Godunov-type LTS solver, the channel is again divided into 250 regularly spaced cells, with spatial increment $\Delta x = 0.1$ m. In solving the one-dimensional shallow water equations, a pair of waves is generated at each interface between adjacent cells, and so a total of (250-1) x 2 = 498 waves are generated from the interior interfaces, neglecting the end boundaries. The tolerance used to assess convergence is set to 1 x 10^{-5}.

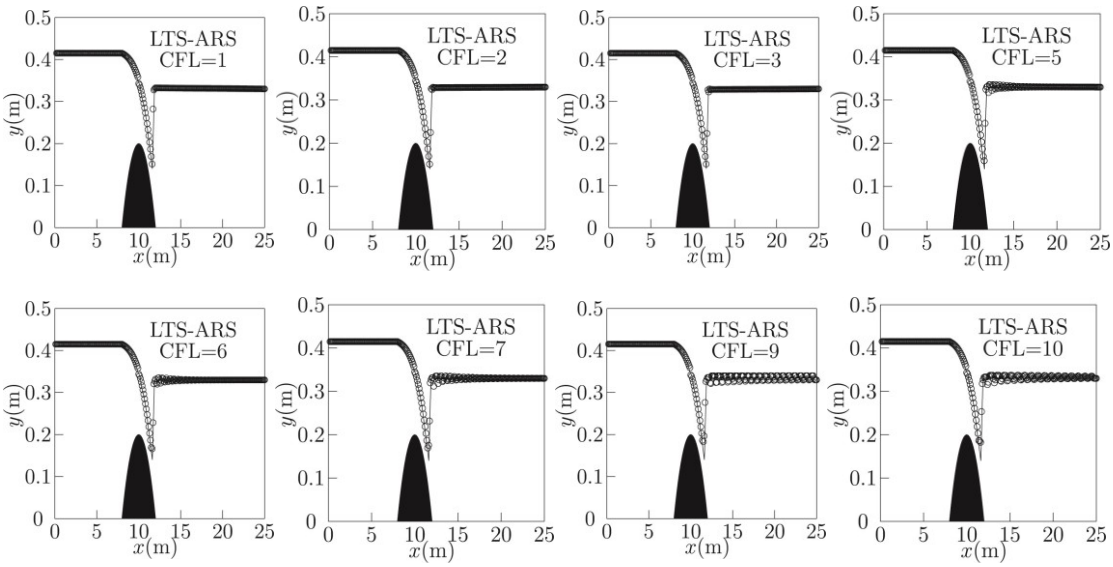

Fig. 13 Transcritical flow over a fixed bed hump: Steady state free surface elevation profiles obtained from analytical solution [33] (solid line) and LTS prediction using Algorithm 2 (open circles).

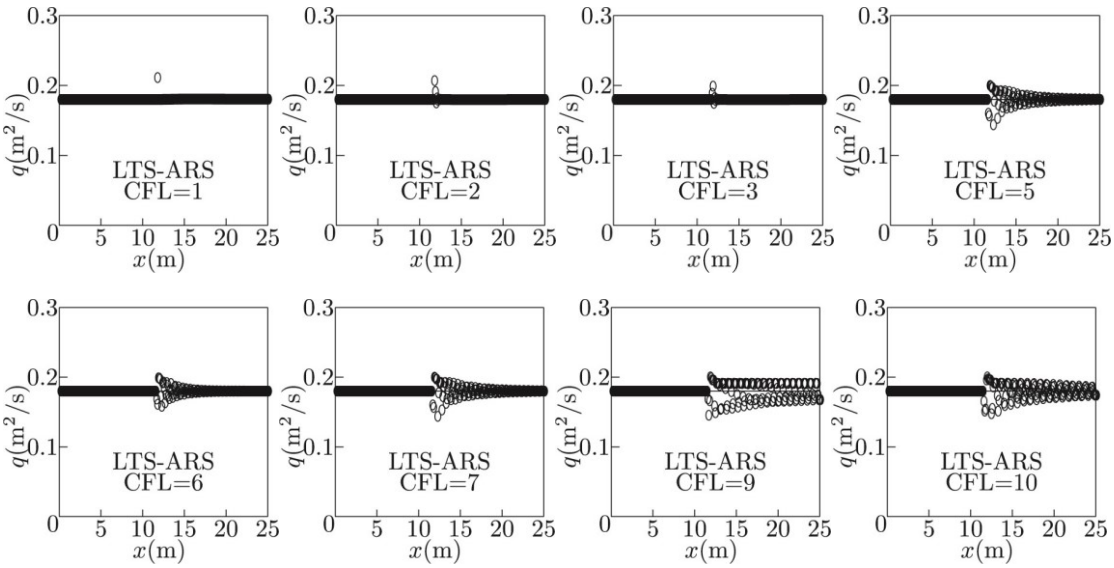

Fig. 14 Transcritical flow over a fixed bed hump: Steady state mass flux profiles obtained from analytical solution [33] (solid line) and LTS prediction using Algorithm 2 (open circles).

Fig. 13 and Fig. 14 compare the numerical predictions by the Godunov-type LTS solver using Algorithm 2 for different values of CFL number against analytical solutions of the steady state water surface profile and the mass flux along the channel. The LTS-predicted water levels are consistently slightly larger than those of the analytical solution upstream of the hump. The hydraulic jump occurs at almost the same location on the downstream slope of the hump, regardless of CFL number, and in agreement with the analytical solution. The exact shape of the hydraulic jump becomes slightly less well defined at the highest values of CFL, with a less prominent minimum depth immediately before the jump and spurious oscillations immediately after the jump. The overall results are satisfactory for CFL < 4. However, the LTS scheme could not converge for CFL = 4, 8, and > 10, and so no results are presented for these cases. The spurious oscillations are increasingly obvious

for CFL > 4, and the results are unacceptable for CFL ≥ 9.

It is relevant to examine the efficiency of the Godunov-type LTS algorithm, which has been implemented on a computer configured as follows:

CPU: Intel Core i9-10900K @ 3.70GHz with overclock
Memory: Kingston DDR4 128GB 3200MHz with XMP opened
SSD: Intel 750 series PCIe interface 1.2TB

Table 8 lists the number of computational steps, CPU time, and average run time per computational step (obtained as the ratio of CPU time to number of steps) required for convergence for different CFL numbers when the flow converged to steady state. The CPU time was calculated as the difference between the run start time and end time of the program. This approach led to ± 0.2 s error in CPU time for different runs of exactly the same case because of the use of random memory blocks and CPU loads auto-arranged by the above computer system. From the table, we can see that the average run time per computational step lies in a narrow range from 3.58×10^{-3} to 3.94×10^{-3} s, indicating that this parameter is relatively insensitive to CFL number (bearing in mind the error introduced by the computer effectively increases at larger CFL numbers).

CFL Number	1	2	3	5	6	7	9	10	Roe
Steps	2966	1763	1177	816	772	1110	411	1173	6099
CPU Time (s)	3.66	2.25	1.59	1.12	1.07	1.57	0.59	1.78	3.01
Time/Step (10^{-3}s)	1.23	1.27	1.35	1.37	1.38	1.41	1.44	1.52	0.49

Table 8 Computational effort by Godunov-type LTS solver for given CFL numbers compared to Roe scheme

As noted above, the numerical simulation does not converge for CFL = 4, and spurious oscillations develop downstream of the hydraulic jump for CFL > 4. We now investigate use of an entropy fix to correct this effect.

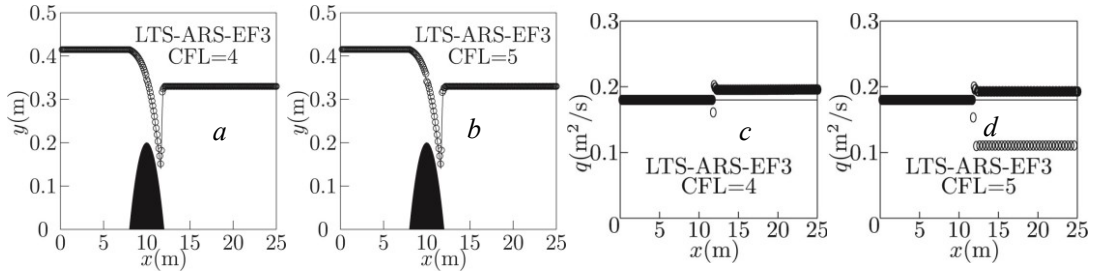

Fig. 15 Transcritical flow over a fixed bed hump: (a) free surface elevation profile for CFL = 4 and δ = 0.2; (b) free surface elevation profile for CFL = 5 and δ = 0.2; (c) mass flux profile for CFL = 4 and δ = 0.2; and (d) mass flux profile for CFL = 5 and δ = 0.2. Analytical solution [33] (solid line) and predicted values using Algorithm 2 (open circles).

The free surface elevation profiles depicted in Fig. 15(a) and (b) show that the numerical predictions using Algorithm 2 provide an almost perfect match to the exact solution. This is not the case for the mass flux profiles in (c) and (d), where the predictions are unsatisfactory immediately downstream of the hydraulic jump, with grid scale fluctuations evident for CFL = 5.

5. Conclusions

Godunov-type Large Time Scheme (LTS) algorithms have been investigated for non-homogeneous Shallow Water Equations (SWEs). In order to incorporate correctly the source term into the LTS algorithm, a new Exact Riemann Solver (ERS) was implemented in LTS (LTS-ERS). We compared LTS-ERS with the LTS algorithm using an existing Approximate Riemann Solver (LTS-ARS) for four cases, all of which possess a bed-slope source term. In the first three cases, comprising open channel flow over a bed containing a step involving two rarefactions, two shock-like bores, and a dam break over a wet bed, satisfactory results were obtained for CFL = 2 by all the new solvers whereas the conventional solvers were unable to obtain stable results for CFL > 1. However, spurious discontinuities and oscillations affected predictions by the LTS-ERS algorithm at higher CFL. Entropy fixes were effective in removing discontinuity in the rarefactions for CFL up to 8, but less successful at eliminating oscillations for larger CFL. Although the oscillations were not fully removed by LTS-ARS in conjunction with entropy fixes when applied to shock-type cases, they were successfully eliminated by LTS-ERS with entropy fixes but at the cost of a shift in the position of shock-like bores. In the fourth case of steady state, transcritical, frictionless flow over a bed hump, satisfactory agreement was also achieved between the predicted free surface profiles and corresponding analytical solution, provided CFL ≤ 3. Oscillations or divergence occurred at higher CFL values when applying LTS-ARS without entropy fixes. The implementation of entropy fixes within the LTS update procedure cured spurious oscillation and divergence, over the range of CFL values considered herein.

The present algorithm requires further development to incorporate additional source terms related to bed friction, wind friction, eddy diffusion, Coriolis acceleration, etc., and its extension to two-dimensions is essential for broader applications in engineering practice. It should be noted that the proposed ERS together with entropy fixes enables the LTS algorithm to achieve more accurate representation of rarefaction waves by reducing spurious oscillations at high CFL number but at the cost of additional dispersion in the shock-like flows. The proposed ERS is designed for a positive step (bed elevation downstream higher than upstream). ERS for a negative step (bed elevation downstream lower than upstream) merits further investigation to broaden application of LTS in practice.

Acknowledgements

This work was supported by the National Natural Science Foundation of China (51509216, 52079120). The authors would like to thank R. Bernetti for providing us with the source code of his paper [28].

APPENDIX: Fourier analysis of LTS scheme

First, Eq (30) is discretized over an LTS step as follows:

$$
\begin{aligned}
u_j^{n+1} &= u_j^n - \sum_{j=1}^{N} \left(\Delta u\right)_j - \zeta \left(\Delta u\right)_{N+1} \\
&= u_j^n - \left[\left(u_j^n - u_{j-1}^n\right) + \left(u_{j-2}^n - u_{j-3}^n\right) + \cdots \quad \left(\quad_{-1} - u_{j-N}^n\right) \right] + \zeta \left(u_{j-N}^n - u_{j-N-1}^n\right) \\
&= u_{j-N}^n - \zeta \left(u_{j-N}^n - u_{j-N+1}^n\right)
\end{aligned}
\tag{A1}
$$

where ζ is determined from Eq. (35). We let $u_j^n = v^k \exp\left(ikx_j\right)$, and substitute into Eq. (A1), giving:

$$
v^{k+1} \exp\left(ikx_j\right) = v^k \exp\left(ikx_{j-N}\right) - \zeta v^k \left[\exp\left(ikx_{j-N}\right) - \exp\left(ikx_{j-N-1}\right) \right] \tag{A2}
$$

Then, the numerical amplification factor is

$$
\begin{aligned}
G &= \exp\left(iNk\Delta x\right) - \zeta \left\{ \exp\left(iNk\Delta x\right) - \exp\left[i\left(N+1\right)k\Delta x \right] \right\} \\
&= \exp\left(iNk\Delta x\right) \left\{ 1 - \zeta \left[1 - \exp\left(-ik\Delta x\right) \right] \right\}
\end{aligned}
\tag{A3}
$$

Setting $\theta = k\Delta x$, then Eq(A3) becomes:

$$
G = \left[\cos\left(N\theta\right) + i\sin\left(N\theta\right) \right] \left\{ 1 - \zeta \left[1 - \left(\cos\theta - i\sin\theta\right) \right] \right\} \tag{A4}
$$

Hence,

$$
\begin{aligned}
\left|G\right| &= \left|\cos\left(N\theta\right) + i\sin\left(N\theta\right)\right| . \left| 1 - \zeta \left[1 - \left(\cos\theta - i\sin\theta\right) \right] \right| \\
&= \left| 1 - \zeta \left[1 - \left(\cos\theta - i\sin\theta\right) \right] \right|
\end{aligned}
\tag{A5}
$$

in which $\left|\cos\left(N\theta\right) + i\sin\left(N\theta\right)\right| = 1$. Then,

$$
\begin{aligned}
\left|G\right|^2 &= \left[1 - \zeta\left(1 - \cos\theta\right) \right]^2 + \left(\zeta\sin\theta\right)^2 \\
&= 1 - 2\left(1 - \cos\theta\right) + \zeta^2 \left(1 - \cos\theta\right)^2 + \left(\zeta\sin\theta\right)^2 \\
&= 1 - 2\left(1 - \cos\theta\right) + \zeta^2 \left(2 - 2\cos\theta\right) \\
&= 1 - 2\left(1 - \zeta^2\right)\left(1 - \cos\theta\right) \\
&= 1 - \left(1 - \zeta^2\right)\sin^2\frac{\theta}{2}
\end{aligned}
\tag{A6}
$$

From Fig. 6 and Eq. (35) we can see $\zeta \le 1$, so the numerical amplification factor $\left|G\right| \le 1$.

When the CFL number is an exact integer, Eq. (A1) simplifies to:

$$
u_j^{n+1} = u_{j-N}^n \tag{A7}
$$

Letting,

$$
u\left(x,t\right) = \exp\left[i\left(kx - \omega t\right) \right] \tag{A8}
$$

and substituting into Eq. (A7) gives:

$$
\exp\left[i\left(kx - \omega\left(t + \Delta t\right)\right) \right] = \exp\left[i\left(k\left(x - N\Delta x\right) - \omega\Delta t\right) \right] \tag{A9}
$$

By definition,

$$\omega\Delta t = Nk\Delta x \tag{A10}$$

and so,

$$\omega = \frac{Nk\Delta x}{\Delta t} = \frac{N\alpha}{\Delta t} = \frac{kaN\alpha}{N\alpha} = ka \tag{A11}$$

The phase velocity is

$$c = \frac{\omega}{k} = a \tag{A12}$$

The wave group velocity is

$$\frac{\mathrm{d}\omega}{\mathrm{d}\alpha} = 0 \tag{A13}$$

References:

[1]. Abbott, M.B. and A.W. Minns, Computational hydraulics. 2nd Edition, 1998, London & New York: Routledge.

[2]. Cunge, J.A., F.M. Holly and A. Verwey, Practical aspects of computational river hydraulics. 1980, London: Pitman.

[3]. Roe, P.L., Approximate Riemann Solvers, Parameter Vectors, and Difference Schemes. Journal of Computational Physics, 1981. 135(2): p. 250 - 258.

[4]. Osher, S. and F. Solomon, Upwind Difference Schemes for Hyperbolic Systems of Conservation Laws. Mathematics of Computation, 1982. 38(Apr.): p. 339--374.

[5]. Harten, A., P.D. Lax and B. van Leer, On Upstream Differencing and Godunov-Type Schemes for Hyperbolic Conservation Laws. Society for Industrial and Applied Mathematics, 1983. 25(1): p. 35--61.

[6].Liou, M. and J.S. Christopher, A new flux splitting scheme, Journal of Computational Physics. 1993. p. 23-39.

[7]. Toro, E.F., Shock-Capturing Methods for Free-Surface Shallow Flows. 2001, John Wiley and Sons: New York.

[8]. Toro, E.F., Riemann Solvers and Numerical Methods for Fluid Dynamics. 3rd Edition. 2009: Springer.

[9]. LeVeque, R.J., Finite-Volume Methods for Hyperbolic Problems. 2004: Cambridge University Press.

[10]. Guinot, V., Godunov-type Schemes an Introduction for Engineers. 2003, Elsevier.

[11]. Toro, E.F. and P. García-Navarro, Godunov-type methods for free-surface shallow flows: A review. Journal of Hydraulic Research, 2007. 45(6): p. 736-751.

[12]. LeVeque, R.J., Large Time Step Shock-Capturing Techniques for Scalar Conservation Laws. SIAM Journal on Numerical Analysis, 1982. 19(6): p. 1091-1109.

[13]. Harten, A., On a Large Time-Step High Resolution scheme, Mathematics of Computation. 1986. 46(5), p. 379-399.

[14]. LeVeque, R.J., High resolution finite volume methods on arbitrary grids via wave propagation. Journal of Computational Physics, 1988. 78(1): p. 36 - 63.

[15]. Murillo, J., P. García-Navarro, P. Brufau, and J. Burguete, Extension of an explicit finite volume

method to large time steps (CFL>1): application to shallow water flows. International Journal for Numerical Methods in Fluids, 2006. 50(1): p. 63--102.
[16]. Qian, Z. and C. Lee, A class of large time step Godunov schemes for hyperbolic conservation laws and applications, in Journal of Computational Physics. 2011. p. 7418-7440.
[17]. Qian, Z. and C. Lee, On large time step TVD scheme for hyperbolic conservation laws and its efficiency evaluation. Journal of Computational Physics, 2012. 231(21): p. 7415-7430.
[18]. Xu, R., D. Zhong, B. Wu, X. Fu, and R. Miao, A large time step Godunov scheme for free-surface shallow water equations. Chinese Science Bulletin, 2014. 59(21): p. 2534-2540.
[19]. Morales-Hernández, M., M.E. Hubbard and P. García-Navarro, A 2D extension of a Large Time Step explicit scheme (CFL>1) for unsteady problems with wet/dry boundaries. Journal of Computational Physics, 2014. 263(April): p. 303 - 327.
[20]. Lindqvist, S., P. Aursand, T. Flåtten, and A.A. Solberg, Large Time Step TVD Schemes for Hyperbolic Conservation Laws. SIAM Journal on Numerical Analysis, 2016. 54(5): p. 2775-2798.
[21]. LeVeque, R.J., Balancing Source Terms and Flux Gradients in High-Resolution Godunov Methods: The Quasi-Steady Wave-Propagation Algorithm. Journal of Computational Physics, 1998. 146(1): p. 346 - 365.
[22]. García-Navarro, P. and E. Vazquez-Cendon M, On numerical treatment of the source terms in the shallow water equations. Computers & Fluids, 2000. 29: p. 951-979.
[23]. Xi, X. and Q. Liang, A new efficient implicit scheme for discretising the stiff friction terms in the shallow water equations. Advances in Water Resources, 2018. 117: p. 87-97.
[24]. Li, J., An h-box Method for Shallow Water Equations. 2019, PhD Dissertation, University of Colombia: USA.
[25]. Murillo, J. and P. García-Navarro, Weak solutions for partial differential equations with source terms: Application to the shallow water equations. Journal of Computational Physics, 2010. 229(11): p. 4327 - 4368.
[26]. Andrianov, N., Performance of numerical methods on the non-unique solution to the Riemann problem for the shallow water equations. International Journal for Numerical Methods in Fluids, 2005. 47(8-9): p. 825 – 831.
[27]. Alcrudo, F. and F. Benkhaldoun, Exact solutions to the Riemann problem of the shallow water equations with a bottom step. Computers & Fluids, 2001. 30(6): p. 643-671.
[28]. Bernetti, R., V.A. Titarev and E.F. Toro, Exact solution of the Riemann problem for the shallow water equations with discontinuous bottom geometry. J. Comput. Phys., 2008. 227(6): p. 3212 – 3243.
[29]. Rosatti, G. and L. Begnudelli, The Riemann Problem for the one-dimensional, free-surface Shallow Water Equations with a bed step: Theoretical analysis and numerical simulations. Journal of computational Physics, 2010. 229(3): p. 760-787.
[30]. Trefethen, L.N., Group Velocity in Finite Difference Schemes. SIAM review, 1982. 24(2): p. 113-136.
[31]. Kundu, A. and S. De, Application of compact schemes in the CUSP framework for strong shock-vortex interaction. Computers & Fluids, 2016. 126: p. 192-204.
[32]. Morales-Hernandez, M. and J. Murillo, A large time step 1D upwind explicit scheme (CFL> 1): Application to shallow water equations. Journal of Computational Physics, 2012. 231: p. 6532-6557.
[33]. Goutal, N. and F. Maurel, Proceedings of the 2nd workshop on dam-break wave simulation. 1997, France: Department Laboratoire National d'Hydraulique, Groupe Hydraulique Fluviale.